A Parameterization of Deformation Fields for Diffeomorphic Image Registration and Its Application to Myocardial Delineation

Hua-mei Chen[1], Aashish Goela[2,3], Gregory J. Garvin[2,4], and Shuo Li[1,2,5]

Department of
[1] Medical Biophysics
[2] Medical Imaging
[3] University Hospital
UWO, London, Ontario
[4] St. Joseph's HealthCare, London, Ontario
[5] GE HealthCare, London, Ontario

Abstract. This study investigates a new parameterization of deformation fields for image registration. Instead of standard displacements, this parameterization describes a deformation field with its *transformation Jacobian* and *curl of end velocity field*. It has two important features which make it appealing to image registration: 1) it *relaxes* the need of an *explicit* regularization term and the corresponding *ad hoc* weight in the cost functional; 2) explicit constraints on transformation Jacobian such as *topology preserving* and *incompressibility* constraints are straightforward to impose in a *unified* framework. In addition, this parameterization naturally describes a deformation field in terms of *radial* and *rotational* components, making it especially suited for processing cardiac data. We formulate diffeomorphic image registration as a constrained optimization problem which we solve with a *step-then-correct* strategy. The effectiveness of the algorithm is demonstrated with several examples and a comprehensive evaluation of myocardial delineation over 120 short-axis cardiac cine MRIs acquired from 20 subjects. It shows competitive performance in comparison to two recent segmentation based approaches.

Keywords: diffeomorphic image registration, topology preserving, incompressibility constraint, cardiac MRI, myocardial delineation.

1 Introduction

Image registration, which consists of establishing point correspondence between two images, is commonly understood as an *ill-posed* problem when stated as the optimization of a similarity metric alone [1]. Without regularization, this may generate multiple physically non-plausible solutions (i.e., rendering tissue folding/tearing in human anatomy studies). Fig. 1 depicts a typical example, where standard gradient descent optimization over displacements was used to minimize the sum of squared difference between the images S (study) and T (template). Fig. 1(c) shows the transformation that generates S from T. Figs. 1(d) and (e) illustrate the mesh folding phenomenon

T. Jiang et al. (Eds.): MICCAI 2010, Part I, LNCS 6361, pp. 340–348, 2010.

from the result. In this study, we investigate a new parameterization of deformation fields which can avoid such undesirable phenomenon (cf. the results in Figs. 1(f) and 1(g)), while affording other important features that make it appealing to image registration. Instead of standard displacements, this parameterization describes a deformation field with its *transformation Jacobian determinant* and *curl of end velocity field*. This relaxes the need of an explicit regularization to produce a physically plausible result because smoothness is implicitly embedded in the solution. Thus, empirical tradeoff between the similarity term and the regularization term, which may cause bias [18], is not necessary. Furthermore, ensuring the deformation to be diffeomorphic, which has spawned a significant amount of recent work [13-16], can be accomplished by directly requiring the transformation Jacobian to be positive. Also, other desirable constraints can be enforced within the *same* framework using explicit restriction on the transformation Jacobian; for instance, the incompressibility constraint requires the Jacobian to be equal to one. In addition, our parameterization naturally describes a deformation field in terms of *radial* and *rotational* components, making it especially suited for processing cardiac data [12]. Fig. 2 illustrates this; it depicts four transformations generated from different pairs of transformation Jacobian m and curl g around the grid center. Obviously, the transformation Jacobian m and curl g are directly related to the radial and rotational components of the deformation field.

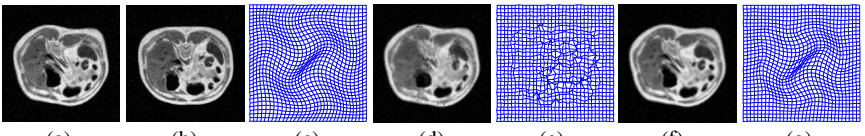

Fig. 1. An illustration of the ill-posed registration problem using conventional deformation parameterization. (a) Study, (b) template, (c) ground truth, (d) deformed template obtained from standard gradient descent optimization over displacements, (e) the deformation field corresponding to (d), (f) deformed template obtained from the proposed parameterization, (g) the deformation field corresponding to (f).

Our parameterization is based on a moving mesh method, originally designed to generate a grid suitable for solving partial differential equations numerically [2-3]. It naturally leads to a formulation of diffeomorphic image registration as a constrained optimization problem which we solve with a *step-then-correct* strategy. Such strategy has been adopted in the Demons algorithm, where unconstrained optimization is followed by Gaussian filtering to impose a smoothness constraint.

The effectiveness of the method is demonstrated with examples of diffeomorphic image registration, registration with an incompressibility constraint, and a comprehensive evaluation of myocardial delineation over 120 short-axis cardiac cine MRIs acquired from 20 subjects. Myocardial delineation is acknowledged as a challenging problem due to large deformations, and has been commonly tackled by segmentation based techniques [6-9]. Our results show favorable performance in comparison to two recent segmentation based approaches. In addition to myocardial delineation, our algorithm yields dense cardiac motion field which is very useful in the diagnosis of cardiovascular diseases [11].

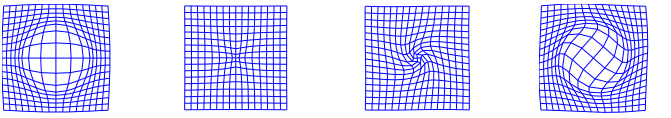

(a) $(m,g)= (10,0)$ (b) $(m,g)= (0.1,0)$ (c) $(m,g)= (0.1,1)$ (d) $(m,g)= (10,-2)$

Fig. 2. Geometrical interpretation of the parameterization with (m, g). It is clear that the transformation Jacobian m and curl g are directly related to the radial and rotational components of the deformation field.

2 Moving Mesh Grid Generation

Our parameterization method is based on the next grid generation theorem [2,3].

Problem 1 *For a given continuous monitor function* $m(\xi):\Omega\to\mathbb{R}$ *constrained by*

$$\int_{\Omega} m = |\Omega|, \tag{1}$$

find a transformation $\varphi:\Omega\to\Omega$, $\partial\Omega\to\partial\Omega$, such that the transformation Jacobian is equal to the given monitor function m. That is,

$$J_{\varphi}(\xi) = m(\xi). \tag{2}$$

The following theorem provides a solution to Problem 1 [2,3].

Theorem 1 *A transformation* φ *constructed by the following steps satisfies eq. (2).*
Step 1: Find a vector field $\eta(\xi)$ *which satisfies:*

$$div\ \eta(\xi) = m(\xi) - 1 \tag{3}$$

with the Neumann boundary condition.
Step 2: Construct an artificial-time dependent velocity vector field via $\eta(\xi)$ *by*

$$v_t(\xi) = \frac{\eta(\xi)}{t + (1-t)m(\xi)}, t\in[0,1] \tag{4}$$

Step 3: The transformation φ *in Problem 1 is the solution of the following ODE evaluated at t = 1,*

$$\frac{d\psi(\xi,t)}{dt} = v_t(\psi(\xi,t)),\ t\in[0,1], \tag{5}$$

with $\psi(\xi, t=0) = \xi$. *That is,* $\varphi(\xi) = \psi(\xi, t=1)$.

Proposed parameterization. The solution to Problem 1 is not unique. Generating a unique solution entails constraining the curl of the vector field $\eta(\xi)$, which is the *end velocity field* $v_1(\xi)$ according to (4), and solving the div-curl system under the *Dirichlet* boundary condition [4]. We replace eq. (3) by the following div-curl system,

$$\begin{cases} div\ \eta(\xi) = m(\xi) - 1 \\ curl\ \eta(\xi) = g(\xi) \end{cases} \tag{3'}$$

with null boundary condition $\eta(\xi) = 0\ \forall \xi \in \partial\Omega$ (i.e., stationary boundary), where $g(\xi)$ is a continuous function over Ω. Hence, a transformation generated by the steps in Theorem 1 can be parameterized with its transformation Jacobian, denoted by $m(\xi)$ $(= J_\varphi(\xi))$, and the curl of the corresponding end velocity field, denoted by $g(\xi)$ $(= \nabla \times \eta(\xi))$. We note that the solution in (3′) is always one degree smoother than *m* and *g*.

3 Constrained Diffeomorphic Image Registration

With the above parameterization, we formulate diffeomorphic image registration as the following constrained optimization problem.

Problem 2. Given two images S and T, defined over $\Omega \subset \mathbb{R}^2$*, find the function pair* $(m(\xi), g(\xi))$, $\xi \in \Omega$*, that optimizes a similarity measure* $E_{Sim}(S, T, \varphi_{m,g})$ *between S and T, subject to the constraints:*

$$\begin{cases} \int_\Omega m = |\Omega| & \text{(6a)} \\ th_{high} > m(\xi) > th_{low}, \quad \xi \in \Omega' \subset \Omega & \text{(6b)} \end{cases}$$

where $th_{low} > 0$ *ensuring that* $\varphi_{m,g}$ *is a diffeomorphism.*

Note that when $th_{low} \approx th_{high}$ (e.g., $th_{low} = 0.99$ and $th_{high} = 1.01$), inequality (6b) effectively imposes the *incompressibility* constraint in a *sub-region* Ω' of the image domain Ω, which is not always possible with existing methods [17]. The parameterization of φ with *m* and *g* is indicated by its subscripts. In the following, we formulate our algorithm for any E_{Sim}, but in the experiments, we use SSD. Next, we present a *step-then-correct* optimization strategy to solve Problem 2.

Algorithm 1. *Given an image pair S (study) and T (template) and* th_{low} *and* th_{high}*, consider the following steps.*

Step 1. Compute unconstrained gradients $\nabla_m E_{Sim}(S, T, \varphi_{m^i, g^i})$ *and* $\nabla_g E_{Sim}(S, T, \varphi_{m^i, g^i})$.

Step 2. a. Terminate if step size $\delta < \delta_{th}$ *or the maximum iteration is reached.*

b. Update (m, g) by

$$m^{i+1} = m^i + \delta \cdot \frac{\nabla_m E_{sim}}{\max |\nabla_m E_{sim}|} \text{ and } g^{i+1} = g^i + \delta \cdot \frac{\nabla_g E_{sim}}{\max |\nabla_g E_{sim}|}.$$

Step 3. a. For each pixel location $\xi \in \Omega' \subset \Omega$*, impose constraint (6b) by*

$$m^{i+1}(\xi) \leftarrow \max(m^{i+1}(\xi), th_{low}) \text{ and } m^{i+1}(\xi) \leftarrow \min(m^{i+1}(\xi), th_{high}).$$

b. For each pixel location $\xi \in \Omega$, *impose constraint (6a) by*

$$m^{i+1}(\xi) \leftarrow m^{i+1}(\xi) \cdot \frac{|\Omega|}{\sum_{\xi \in \Omega} m^{i+1}(\xi)}.$$

Step 4. Use Theorem 1 with (3') to compute $\varphi_{m^{i+1}, g^{i+1}}$ *and update* E_{Sim}. *If it improves,* $i \leftarrow i+1$, *go to Step 1; otherwise, decrease* δ *and go to Step 2.*

4 Numerical Methods

2D Div-curl solver. We converted div-curl system (3′) into two Poisson equations [5]

$$\begin{cases} \Delta \eta^x = m_x - g_y \equiv F^1 & \text{(7a)} \\ \Delta \eta^y = m_y + g_x \equiv F^2 & \text{(7b)} \end{cases}$$

and used a FFT based Poisson solver to find η efficiently under the null boundary condition. The superscripts denote different components and the subscripts partial derivatives. Euler method with 20 time steps was used in (5) to compute the transformation φ from η via eqs. (4) and (5).

Conversion of unconstrained gradients. Discretizing the image domain and applying the chain rule repeatedly result in

$$\begin{aligned} \frac{\partial E_{Sim}}{\partial m(I_j)} = & \sum_{l \in N(k)} \frac{\partial E_{Sim}}{\partial \varphi^x(I_l)} \frac{\partial \varphi^x(I_l)}{\partial \eta^x(I_l)} \sum_{k \in N(j)} \frac{\partial \eta^x(I_l)}{\partial F^1(I_k)} \frac{\partial F^1(I_k)}{\partial m(I_j)} \\ & + \sum_{l \in N(k)} \frac{\partial E_{Sim}}{\partial \varphi^y(I_l)} \frac{\partial \varphi^y(I_l)}{\partial \eta^y(I_l)} \sum_{k \in N(j)} \frac{\partial \eta^y(I_l)}{\partial F^2(I_k)} \frac{\partial F^2(I_k)}{\partial m(I_j)}, \end{aligned} \tag{8}$$

and a similar expression for $\frac{\partial E_{Sim}}{\partial g(I_j)}$. In (8), I_j is the j^{th} grid point and the notation $k \in N(j)$ indicates that I_k belongs to some neighborhood of I_j. Each partial derivative term and the size of each neighborhood depend on the actual numerical implementation as explained below.

The terms $\frac{\partial E_{sim}}{\partial \varphi^x}$ and $\frac{\partial E_{sim}}{\partial \varphi^y}$ constitute the conventional gradient of a cost function parameterized by displacements, which has been studied extensively. Next, $\frac{\partial \varphi^x}{\partial \eta^x}$ and $\frac{\partial \varphi^y}{\partial \eta^y}$ are approximated by the following Euler 1-step integration

$$\varphi(\xi, 1) = \varphi(\xi, 0) + v_1(\varphi(\xi, 0)) = \xi + \eta(\xi), \tag{9}$$

which leads to $\frac{\partial \varphi^x}{\partial \eta^x} = \frac{\partial \varphi^y}{\partial \eta^y} = 1$. The terms $\frac{\partial \eta^x}{\partial F^1}$, $\frac{\partial \eta^y}{\partial F^2}$ and $N(k)$ are determined by eqs.(7). Since η^x and η^y are the solutions of the Poisson equations $\Delta \eta^x = F^1$ and $\Delta \eta^y = F^2$, the neighborhood of I_k (influence zone of varying $F^1(I_k)$ and $F^2(I_k)$ on η^x and η^y respectively) is the whole image domain and the values $\frac{\partial \eta^x(I_l)}{\partial F^1(I_k)}$ and $\frac{\partial \eta^y(I_l)}{\partial F^2(I_k)}$ are the

values of the response of Δ^{-1} operator at I_l due to an impulse at I_k. Next, $\frac{\partial F^1}{\partial m}$, $\frac{\partial F^2}{\partial m}$ and $N(j)$ are again determined by eqs.(7). Using central finite difference to define the derivatives of m, $N(j)$ can be determined as the 3×3 neighborhood of I_j and the values of $\frac{\partial F^1(I_k)}{\delta m(I_j)}$ and $\frac{\partial F^2(I_k)}{\delta m(I_j)}$ are determined by difference operators D_x and D_y given by

$$D_x = \frac{1}{2}\cdot[1 \quad 0 \quad -1] \text{ and } D_y = D_x^T \tag{10}$$

From the above discussion, we conclude that

$$\begin{cases} \nabla_m E_{Sim} = \Delta^{-1}(\nabla_x E_{Sim}) \otimes D_x + \Delta^{-1}(\nabla_y E_{Sim}) \otimes D_y & \text{(11a)} \\ \nabla_g E_{Sim} = \Delta^{-1}(\nabla_x E_{Sim}) \otimes -D_y + \Delta^{-1}(\nabla_y E_{Sim}) \otimes D_x & \text{(11b)} \end{cases}$$

with $\otimes$ denoting the discrete convolution operator and Δ^{-1} the inverse Laplacian operator (Poisson solver).

5 Experimental Results

Diffeomorphic Registration. We first summarize in Table 1 the complete results of the experiment given in Fig. 1. When no noise was added, no mesh folding was observed when the diffeomorphic constraint (DC) was not imposed (e.g., set (th_{low}, th_{high}) = (-20, 20)). Results shown in Fig. 1 correspond to this case. However, with Gaussian noise (std = 0.05) added, mesh folding occurred as indicated by the negative Jacobian and the large maximum error in Table I. Setting (th_{low}, th_{high}) = (0.51, 1.34), which were the ground truth values from the deformation shown in Fig. 1(c), not only effectively prevented the mesh from folding, but also reduced registration errors. This suggests that when a proper *prior* knowledge of Jacobian is available, more *reliable and accurate* registration result can be attained. Notice that the min and max transformation Jacobians obtained in this case (i.e., 0.49 and 1.37 respectively) were close to the pre-set values 0.51 and 1.34. No significant differences were observed by setting different (th_{low}, th_{high}) values (e.g., 0.2 and 2).

Table 1. Numerical result of the diffeomorphic registration experiment

	ssd	**max error (in pixel)**	**mean error (in pixel)**	**max Jacobian**	**min Jacobian**
before registration	3789	7.80	4.75	1.34 (ground truth)	0.51 (ground truth)
noiseless, w/o DC	29	3.17	0.52	1.98	0.06
noisy, w/o DC	250	11.47	0.75	2.01	-1.16
noisy, with DC	246	3.45	0.70	1.37	0.49

Simulated CE-MRI Experiment. The second experiment demonstrates the effectiveness of the proposed method in imposing incompressibility constraint using two

digital phantoms shown in Figs. 3(a) and (b). They simulated pre- and post contrast enhanced (CE) breast MR images. Two sets of thresholds (th_{low}, th_{high}) = (0.1, 10) and (0.99, 1.01) were used in Algorithm 1 to produce the results in Figs. 3(d),3(e),and Figs. 3(f) and 3(g) respectively. Figs. 3(d) and 3(f) are the absolute difference images after registration, and Figs. 3(e) and (g) show the magnified mesh near the simulated cancerous tissues. As a reference, the absolute difference image before registration is provided in Fig. 3(c). The uniformity of the cell sizes in 3(g) indicates that the incompressibility constraint was properly enforced with (th_{low}, th_{high}) = (0.99, 1.01).

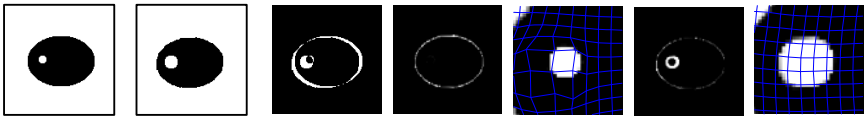

Fig. 3. A simulated contrast enhanced breast MRI experiment to demonstrate the effectiveness of the proposed algorithm in imposing incompressibility constraint

Table 2. Numerical results in terms of Dice Metric (DM) and efficiency

Performance measure	DM (Endo)	DM (Epi)	Average time/frame (sec)
Proposed method	0.93±0.04	0.96±0.01	0.55
Method in [level set]	0.88±0.09	0.94±0.04	6.5
Method in [graph cut]	0.91±0.04	N/A	0.08

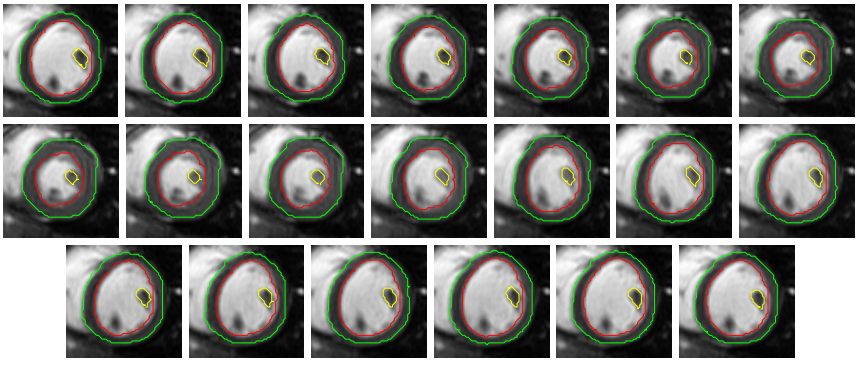

Fig. 4. A complete cardiac cine MRI (left to right, top to bottom) illustrating the tracking of epicardial border (green), endocardial border, and the profile of a papillary muscle (yellow)

Automated Myocardial Borders Delineation. Accurate myocardial borders delineation in cardiac cine MRIs is important in the diagnosis of cardiovascular diseases [6-12]. It yields many significant measures like ejection fraction and radial displacement. In this comprehensive experiment, we used 120 short-axis cardiac cine MRIs clinically

obtained from 20 subjects, including apical, mid-cavity, and basal segments, acquired by 1.5T MRI scanners with fast imaging employing steady state acquisition (FIESTA) mode. For each cine MRI consisting of 20 frames, the first frame was used as the study image S and each of rest frames the template T successively. Each registration result *propagates* to initialize the next registration. As a fair comparison to the segmentation based techniques described in [6-7], our registration based approach did not incorporate a temporal constraint, which can be added by using temporal Bspline basis functions [10], or by recursive Bayesian filtering [11]. The deformation fields obtained were then applied to propagate the manually obtained endo- and epicardium borders from the first frame of each cine MRI. Values of th_{low} and th_{high} were set to be 0.25 and 4 respectively. The maximum number of iteration was fixed at 25 and δ_{th} was set to be 0.01 in all cases. Propagated borders were compared to the ones manually delineated independently by an expert. We also ran the codes described in [6-7] to contrast the accuracies in Table 2, in term of *Dice Metric* (DM), defined as $\frac{2\mathbf{V}_{am}}{\mathbf{V}_a+\mathbf{V}_m}$, where $\mathbf{V}_{\mathrm{a}}$, $\mathbf{V}_{\mathrm{m}}$ and $\mathbf{V}_{\mathrm{am}}$ are the automatically, manually delineated volumes, and the overlap of them respectively. Table 2 shows that our registration based approach yielded the highest *DM* values (higher means closer to manual ones) among the three methods. In addition, our method is very efficient (less than 0.6 sec/frame or 10.5 sec/sequence) which is acceptable for clinical practice. Our platform was HP xw6600 Workstation with 2.83 GHz Intel Xeon CPU with 3.25 GB RAM under Windows XP. All registration codes were written in MATLAB. Although the computational time is higher then the graph cuts based method described in [7], our method produces *dense deformation fields* that can be used to track any features present in the image sequences and provides a means for strain analysis [10], which is not possible using segmentation based approaches. We illustrate this advantage in Fig. 4 by showing a representative cine MRI with not only the automatic delineated epi- and endocardial borders superimposed, but also with the profiles of a papillary muscle (a papillary muscle profile was manually delineated in the first frame). Extension to volume data registration is straightforward, since the underlying moving mesh based grid generation method was originally demonstrated in 3D [2-3].

References

1. Modersitzki, J.: Numerical Methods for Image Registration. Oxford University Press, Oxford (2004)
2. Liao, G., Anderson, D.: A New Approach to Grid Generation. Applicable Analysis 44(3), 285–298 (1992)
3. Liu, J.: New Developments of the Deformation Method. PhD dissertation. Department of Mathematics, The University of Texas at Arlington (2006)
4. Zhou, X.: On Uniqueness Theorem of a Vector Function. Progress in Electromagnetics Research 65, 93–102 (2006)
5. Jiang, B.-N.: The Least-Squares Finite Element Method: Theory and Applications in Computational Fluid Dynamics and Electromagnetics. Springer, Heidelberg (1998)
6. Ben Ayed, I., Li, S., Ross, I.: Embedding Overlap Priors in Variational Left Ventrical Tracking. IEEE Transactions on Medical Imaging 28(12), 1902–1913 (2009)

7. Ben Ayed, I., Punithakumar, K., Li, S., Islam, A.: Left Ventricle Segmentation via Graph Cut Distribution Matching. In: Yang, G.-Z., Hawkes, D., Rueckert, D., Noble, A., Taylor, C. (eds.) MICCAI 2009. LNCS, vol. 5762, pp. 901–909. Springer, Heidelberg (2009)
8. Lynch, M., Ghita, O., Whelan, P.F.: Segmentation of the Left Ventricle of the Heart in 3-D+t MRI Data Using an Optimized Nonrigid Temporal Model. IEEE Trans. on Medical Imaging 27(2), 195–203 (2008)
9. Jolly, M.-P.: Automatic Segmentation of the Left Ventricle in Cardiac MR and CT Images. International Journal of Computer Vision 70(2), 151–163 (2006)
10. Ledesma-Carbayo, M., et al.: Spatio-Temporal Nonrigid Registration for Ultrasound Cardiac Motion Estimation. IEEE Transactions on Medical Imaging 24(9), 1113–1126 (2005)
11. Punithakumar, K., et al.: Heart Motion Abnormality Detection via an Information Measure and Bayesian Filtering. In: Yang, G.-Z., Hawkes, D., Rueckert, D., Noble, A., Taylor, C. (eds.) MICCAI 2009. LNCS, vol. 5762, pp. 373–380. Springer, Heidelberg (2009)
12. Noble, N., et al.: Myocardial Delineation via Registration in a Polar Coordinate System. In: Dohi, T., Kikinis, R. (eds.) MICCAI 2002. LNCS, vol. 2488, pp. 651–658. Springer, Heidelberg (2002)
13. Beg, M., Miller, M., Trouve, A., Younes, L.: Computing Large Deformation Metric Mappings via Geodesic Flows of Diffeomorphism. International Journal of Computer Vision 61(2), 139–157 (2005)
14. Rueckert, D., et al.: Diffeomorphic Registration Using B-Splines. In: Larsen, R., Nielsen, M., Sporring, J. (eds.) MICCAI 2006. LNCS, vol. 4191, pp. 702–709. Springer, Heidelberg (2006)
15. Ashburner, J.: A Fast Diffeomorphic Image Registration Algorithm. NeuroImage 38, 95–113 (2007)
16. Vercauteren, T., Pennec, X., Perchant, A., Ayache, N.: Non-Parametric Diffeomorphic Image Registration with the Demons Algorithm. In: Ayache, N., Ourselin, S., Maeder, A. (eds.) MICCAI 2007, Part II. LNCS, vol. 4792, pp. 319–326. Springer, Heidelberg (2007)
17. Saddi, K., Chefd'hotel, C., Cheriet, F.: Large deformation registration of contrast-enhanced images with volume-preserving constraint. In: Proc. of SPIE Medical Imaging, vol. 6512(1) (2007)
18. Rohlfing, T.: Transformation model and constraints cause bias in statistics on deformation fields. In: Larsen, R., Nielsen, M., Sporring, J. (eds.) MICCAI 2006. LNCS, vol. 4190, pp. 207–214. Springer, Heidelberg (2006)